



Article

Low-Pressure Plasma-Processed Ruthenium/Nickel Foam Electrocatalysts for Hydrogen Evolution Reaction

Chen Liu ^{1,2}, Chia-Yun Tseng ^{1,2}, Ying-Chyi Wang ^{1,2}, I-Chun Cheng ^{3,4}  and Jian-Zhang Chen ^{1,2,4,5,*} 

¹ Graduate Institute of Applied Mechanics, National Taiwan University, Taipei City 10617, Taiwan; r09543009@ntu.edu.tw (C.L.); r10543033@ntu.edu.tw (C.-Y.T.); r10543002@ntu.edu.tw (Y.-C.W.)

² Advanced Research Center for Green Materials Science and Technology, National Taiwan University, Taipei City 10617, Taiwan

³ Department of Electrical Engineering, Graduate Institute of Photonics and Optoelectronics, National Taiwan University, Taipei City 10617, Taiwan; iccheng@ntu.edu.tw

⁴ Innovative Photonics Advanced Research Center (i-PARC), National Taiwan University, Taipei City 10617, Taiwan

⁵ Graduate School of Advanced Technology, National Taiwan University, Taipei City 10617, Taiwan

* Correspondence: jchen@ntu.edu.tw; Tel.: +886-2-3366-5694

Abstract: In this paper, low-pressure 95%Ar–5%H₂, pure Ar, and 95%Ar–5%O₂ plasmas were used for post-treatment of ruthenium (Ru) deposited on nickel foam (NF) (Ru/NF). Ru/NF was then tested as a catalyst for a hydrogen evolution reaction. Significant improvement in electrocatalytic activity with the lowest overpotential and Tafel slope was observed in an alkaline electrolyte (1 M KOH) with 95%Ar–5%O₂ plasma processing on Ru/NF. Linear scanning electrical impedance spectroscopy (EIS) and cyclic voltammetry (CV) also indicate the lowest interfacial impedance and largest electrical double layer capacitance. Experimental results with 0.1 M phosphate buffered saline (PBS) and 0.5 M H₂SO₄ electrolytes were also demonstrated and compared.



Citation: Liu, C.; Tseng, C.-Y.; Wang, Y.-C.; Cheng, I.-C.; Chen, J.-Z.

Low-Pressure Plasma-Processed Ruthenium/Nickel Foam Electrocatalysts for Hydrogen Evolution Reaction. *Materials* **2022**, *15*, 2603. <https://doi.org/10.3390/ma15072603>

Academic Editor: Laura Calvillo

Received: 9 March 2022

Accepted: 30 March 2022

Published: 1 April 2022

Publisher's Note: MDPI stays neutral with regard to jurisdictional claims in published maps and institutional affiliations.



Copyright: © 2022 by the authors. Licensee MDPI, Basel, Switzerland. This article is an open access article distributed under the terms and conditions of the Creative Commons Attribution (CC BY) license (<https://creativecommons.org/licenses/by/4.0/>).

Keywords: hydrogen evolution reaction; plasma; catalyst; ruthenium (Ru); electrolysis

1. Introduction

The global energy demand is continuously increasing owing to rapid industrial development. The global average annual power generation is approximately 2520 GW and annual growth rate of power generation is 2.5% [1]. The extensive use of fossil fuels, such as coal, oil, and natural gas, has dramatically increased carbon dioxide emissions and, in turn, made global warming an increasingly serious concern [2]. To mitigate global warming, alternative energy sources such as renewable energy are being actively explored owing to their smaller carbon footprint. Hydrogen energy is considered one of the most promising alternative energy sources. It involves the storage of energy in the form of chemical bonds and the use of fuel cells (or other equipment) to generate electricity for end-users when needed [3].

Water electrolysis with renewable energy is a green and economical method for producing hydrogen. Platinum (Pt) is the most commonly used catalyst for the hydrogen evolution reaction (HER) of water electrolysis. One main drawback of Pt is its high cost. Over the last 10 years, ruthenium (Ru) has, on average, been 13 times cheaper than Pt [4,5]. Further, Ru and Pt have chemical bonds of similar strength and Ru has a similar ability to dissociate water [6,7]. Therefore, in this study, we investigate Ru as a highly efficient and low-cost catalyst for HER. Previous studies have noted that oxygen (O₂) plasma treatment can produce defects on the catalyst surface and create an oxygen-incorporated structure on the catalysts [8–10]. These improve the electrocatalytic activity of the catalysts. Some studies have shown that argon (Ar) or hydrogen (H₂) plasma treatment has a similar effect [10,11]. In this study, we investigated an Ru catalyst on a nickel foam (NF) electrode (hereafter called the Ru/NF electrocatalyst) with different types of plasma treatments.

An ideal electrocatalyst for HER should work efficiently under a wide range of electrolyte pH values, just like traditional Pt-based catalysts [12–14]. Although neutral aqueous electrolytes are ecofriendly [15] and cause less damage to electrocatalysts, they have hardly been investigated [16]. Electrocatalysts in acidic aqueous electrolytes exhibit high efficiency for generating H₂ and have therefore been widely investigated in recent years [17–26]. However, electrocatalysts in alkaline aqueous electrolytes are used most widely in the industry because the lower vapor pressure of the electrolyte solution makes them more economical [25,27]. Additionally, owing to the low-corrosion environment, the electrocatalysts have a longer lifetime [28]. In this study, low-pressure 95%Ar–5%H₂, pure Ar, and 95%Ar–5%O₂ plasmas were used for post-treatment of Ru/NF electrocatalysts that were then used for water electrolysis. Different electrolyte solutions with various pH values were tested.

2. Experimental Section

2.1. Materials and Regents

For this study, 1.7 mm-thick NF was purchased from HOMOYTECH, Taiwan. Sulfuric acid (H₂SO₄, purity: 95–97%) and acetone (ACE, purity: 99%) were purchased from AUECC, Taipei City, Taiwan. Ethanol (purity: 95%) was purchased from Echo Chemical, Miaoli County, Taiwan. Ethylene glycol (EG, purity: 99%) was purchased from SHOWA, Tokyo, Japan. Ruthenium (III) chloride hydrate (RuCl₃ · H₂O), potassium hydroxide (KOH, purity: 85%), and phosphate-buffered saline (PBS) powders were purchased from Sigma-Aldrich, St. Louis, MO, USA. Unless otherwise stated, all chemicals were used as received without any further purification.

2.2. Synthesis of Ru Electrocatalysts

The untreated NF is named pristine NF. NF (4.0 cm × 3.0 cm × 0.17 cm) was first immersed in a 0.1 M H₂SO₄ solution with ultrasonication for 20 min to remove native oxides on the surface. Then, the NF was sequentially immersed in de-ionized (DI) water, alcohol, and ACE with ultrasonication for 20 min [29]. The resulting NF is denoted as NF*. Then, 0.08 g of RuCl₃ was dissolved in a solution consisting of 20 mL of EG and 20 mL of DI water. Subsequently, NF* was immersed in the solution inside a Teflon-lined autoclave that was sealed and heated at 90 °C for 2 h. The Ru on NF* was then rinsed with DI water and calcined in a furnace at 60 °C for 10 min [5]. The resulting electrode is denoted as Ru/NF*. Finally, low-pressure plasmas of different gases—pure Ar, 95% Ar + 5% H₂, and 95% Ar + 5% O₂—were used to post-treat Ru/NF*. The resulting products were named Ru/NF*—A, Ru/NF*—AH, and Ru/NF*—AO, respectively.

2.3. Characterization

X-ray diffraction (Bruker D2 PHASER XRD) was performed in the 2θ range of 10°–90° with Cu Kα radiation (λ = 0.154060 nm). The water contact angles were measured using a goniometer (Sindatek, Taipei City, Taiwan, Model 100SB). The morphology and chemical composition were characterized by scanning electron microscopy (SEM, JSM-IT100, JEOL) with energy-dispersive X-ray spectrometry (EDS) and X-ray photoelectron spectroscopy (XPS, Thermo Scientific, Waltham, MA, USA, Theta Probe). A low-pressure plasma machine (Harrick, Plasma Cleaner PDC-32G, New York, NY, USA) was used with a pressure of 0.6 torr, flow rate of 8 sccm, and power of 7 W. An electrochemical workstation (Autolab PGSTAT204, Metrohm, Utrecht, The Netherlands) was used to perform cyclic voltammetry (CV; −0.25–0.05 V, potential scan speed: 20–300 mV/s), linear sweep voltammetry (LSV; scanning rate: 5 mV/s), and electrochemical impedance spectroscopy (EIS; 0.1–100,000 Hz) measurements in a three-electrode configuration to characterize the electrocatalyst. Ag/AgCl was used as the reference electrode and platinum (Pt) as the counter electrode. The potential E was then converted to the reverse hydrogen electrode (RHE) by E (vs. RHE) = E (vs. Ag/AgCl) + 0.059 × pH + 0.197 [30,31]. The HER performance of the electrocatalyst was evaluated in three different pH electrolytes. Then, 1 M

KOH aqueous solution ($\text{pH} \approx 14$), 0.5 M H_2SO_4 aqueous solution ($\text{pH} \approx 0$), and 0.1 M phosphate buffer solution (PBS, $\text{pH} \approx 7$) were used as the alkaline, acidic, and neutral electrolyte, respectively.

3. Results and Discussion

3.1. Water Contact Angle

Figure 1(a-1) shows the water contact angle of the pristine NF right after the droplet was dispensed. The water contact angle of pristine NF was 72.1° ; after 42 s, the droplet completely penetrated the NF substrate, as shown in Figure 1(a-2). Figure 1b–f show the water contact angles of NF^* , NF^* , Ru/NF^* , $\text{Ru}/\text{NF}^*\text{-A}$, $\text{Ru}/\text{NF}^*\text{-AH}$, and $\text{Ru}/\text{NF}^*\text{-AO}$; the droplets immediately penetrated the H_2SO_4 -treated NF and all plasma-treated Ru/NF^* . This is attributed to the removal of the native oxide by H_2SO_4 treatment. This could reduce the electron transfer impedance. Further, better hydrophilicity could promote interfacial contacts between the electrolyte and the electrocatalysts [32], thus increasing the electrolyte–electrocatalyst interfacial reactive area and leading to improved performance.

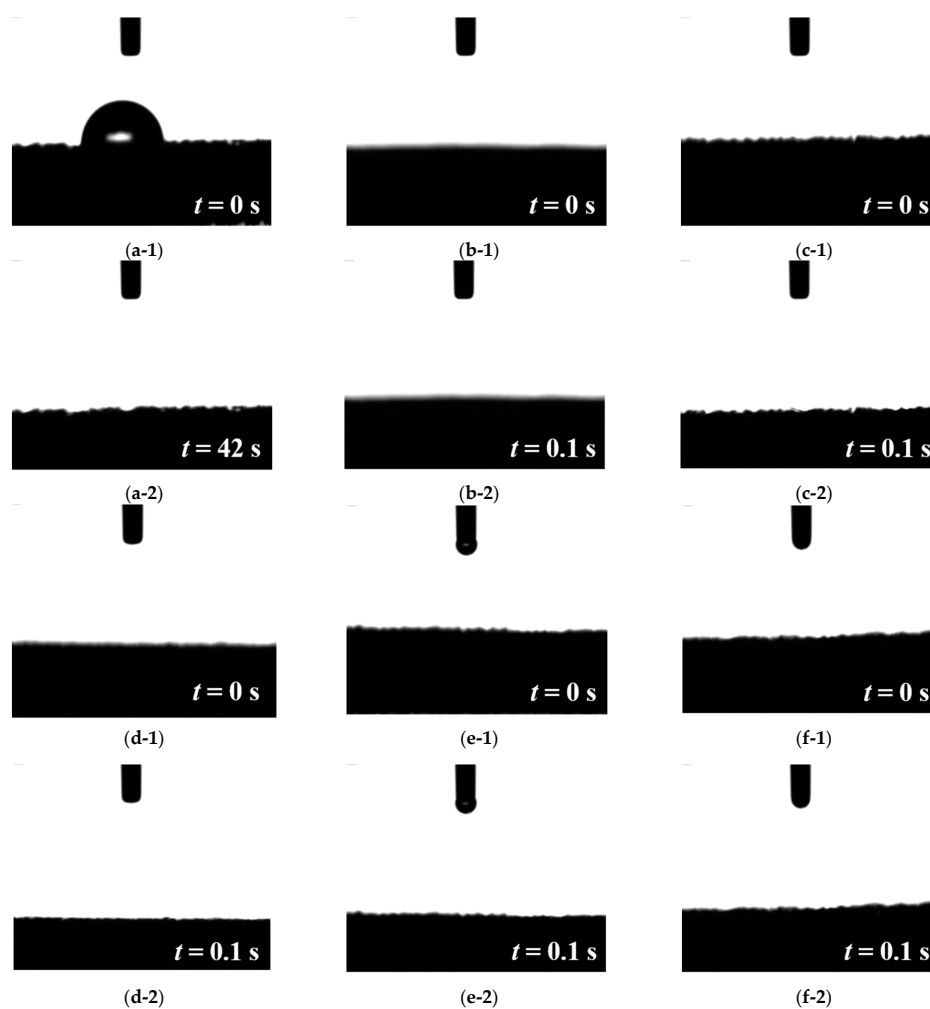


Figure 1. Water contact angles of (a-1) pristine NF right after the droplet was dispensed, (a-2) pristine NF after the droplet was dispensed for 42 s, (b-1) NF^* right after the droplet was dispensed, (b-2) NF^* after the droplet was dispensed for 0.1 s, (c-1) Ru/NF^* right after the droplet was dispensed, (c-2) Ru/NF^* after the droplet was dispensed for 0.1 s, (d-1) $\text{Ru}/\text{NF}^*\text{-A}$ right after the droplet was dispensed, (d-2) $\text{NF}^*\text{-A}$ after the droplet was dispensed for 0.1 s, (e-1) $\text{Ru}/\text{NF}^*\text{-AH}$ right after the droplet was dispensed, and (e-2) $\text{Ru}/\text{NF}^*\text{-HO}$ after the droplet was dispensed for 0.1 s; (f-1) $\text{Ru}/\text{NF}^*\text{-AO}$ right after the droplet was dispensed, and (f-2) $\text{Ru}/\text{NF}^*\text{-AO}$ after the droplet was dispensed for 0.1 s.

3.2. SEM

Figure 2 shows the SEM images of the pristine NF, NF*, Ru/NF*, Ru/NF*-A, Ru/NF*-AH, and Ru/NF*-AO, respectively. The higher-magnification SEM images with pristine NF and NF* reveal the smooth structure of the surface Figure 2a,b. Figure 2c shows a thick Ru layer with a little fractal structure [5]. In comparison to Ru/NF*, the SEM images of the electrocatalysts with plasma treatment show a few more physical defects, especially more cracks, on the surface (Figure 2d–f).

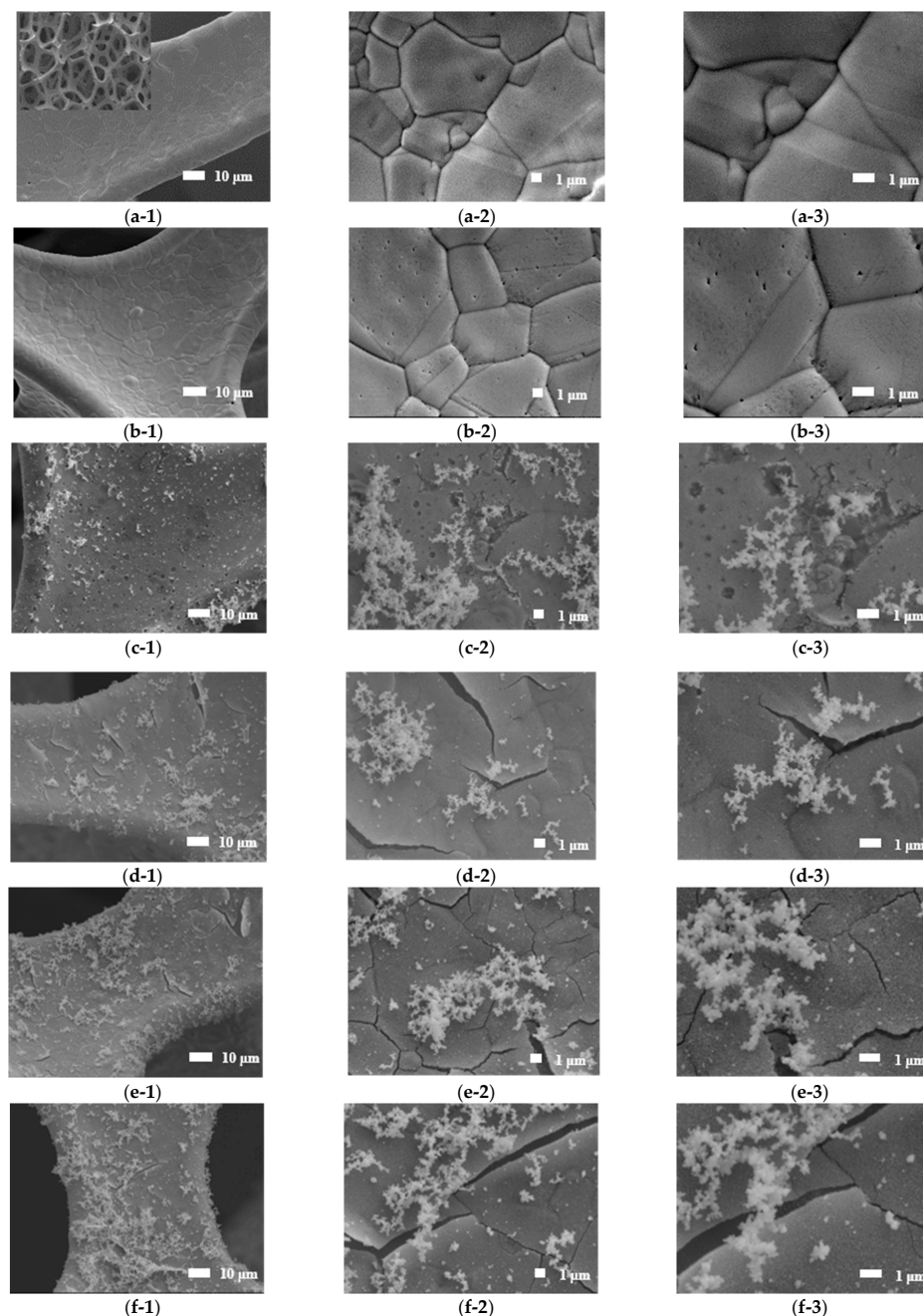


Figure 2. SEM images of pristine NF with (a-1) 1000 \times , (a-2) 5000 \times , and (a-3) 10,000 \times magnification; NF* with (b-1) 1000 \times , (b-2) 5000 \times , and (b-3) 10,000 \times magnification; Ru/NF* with (c-1) 1000 \times , (c-2) 5000 \times , and (c-3) 10,000 \times magnification; Ru/NF*-A with (d-1) 1000 \times , (d-2) 5000 \times , and (d-3) 10,000 \times magnification; Ru/NF*-AH with (e-1) 1000 \times , (e-2) 5000 \times , and (e-3) 10,000 \times magnification; and Ru/NF*-AO with (f-1) 1000 \times , (f-2) 5000 \times , and (f-3) 10,000 \times magnification.

3.3. XRD

Figure 3 shows the XRD patterns of the pristine NF, NF*, Ru/NF*, Ru/NF*-A, Ru/NF*-AH, and Ru/NF*-AO. Strong diffraction peaks are seen at 44.5°, 52.0°, and 76.4°; these correspond to the face-centered cubic (FCC) structure of the NF [5,33]. No peaks of metallic ruthenium or ruthenium oxide were detected, probably because of their low content [5,34].

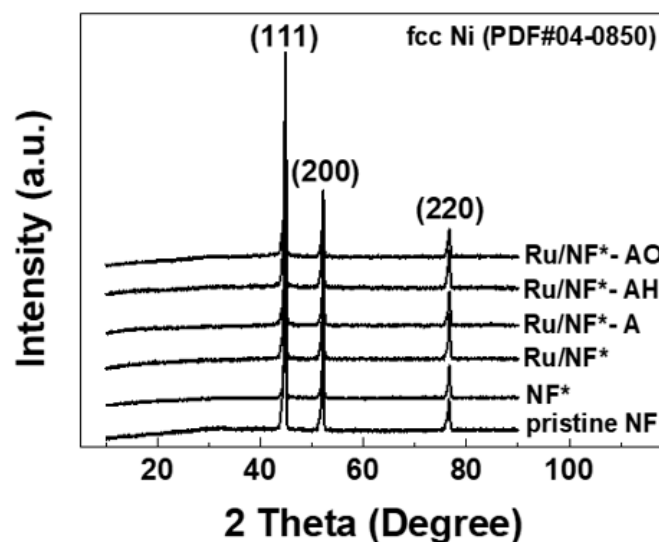


Figure 3. XRD patterns of the pristine NF, NF*, Ru/NF*, Ru/NF*-A, Ru/NF*-AH, and Ru/NF*-AO.

3.4. EDS and XPS

Figure 4 and Table 1 show the EDS results. EDS results of Ru/NF*, Ru/NF*-A, Ru/NF*-AH, and Ru/NF*-AO reveal the deposition of an Ru layer on NF. The oxygen content in Ru/NF* decreased after 100% Ar and 95% Ar–5% H₂ plasma treatment. Chemical elements were also determined by XPS. Figures S1–S4 (Supplementary Materials) show the XPS results. The Ru3d spectra and EDS spectra indicate the successful deposition of Ru. Because metallic nickel is more chemically active than Ru, the NF substrate can spontaneously act as an electron donor for the Ru layer. The accumulation of negative charges on the Ru surface can lead to a higher work function and increase the reduction activity, thereby accelerating the HER process [4,5]. Ru deposited on NF could greatly improve the HER, as discussed below in Section 3.5.

Table 1. Elemental analysis of EDS spectra of pristine NF, NF*, Ru/NF*, Ru/NF*-A, Ru/NF*-AH, and Ru/NF*-AO.

| | Element (wt.%) | | | | |
|-------------|----------------|------|-----|-----|-----|
| | Ni | Ru | O | C | Cl |
| Pristine NF | 96.1 | - | 3.9 | - | - |
| NF* | 91.8 | - | 8.2 | - | - |
| Ru/NF* | 37.0 | 49.4 | 5.6 | 7.0 | 1.0 |
| Ru/NF*-A | 49.0 | 42.7 | 2.8 | 4.9 | 0.7 |
| Ru/NF*-AH | 45.7 | 46.9 | 3.0 | 3.4 | 1.0 |
| Ru/NF*-AO | 34.3 | 56.5 | 5.3 | 3.0 | 1.1 |

After cleaning procedure with 0.1 M H₂SO₄, DI water, alcohol, and ACE. A: Plasma treatment with 100% Ar. AH: Plasma treatment with 95% Ar + 5% H₂. AO: Plasma treatment with 95% Ar + 5% O₂.

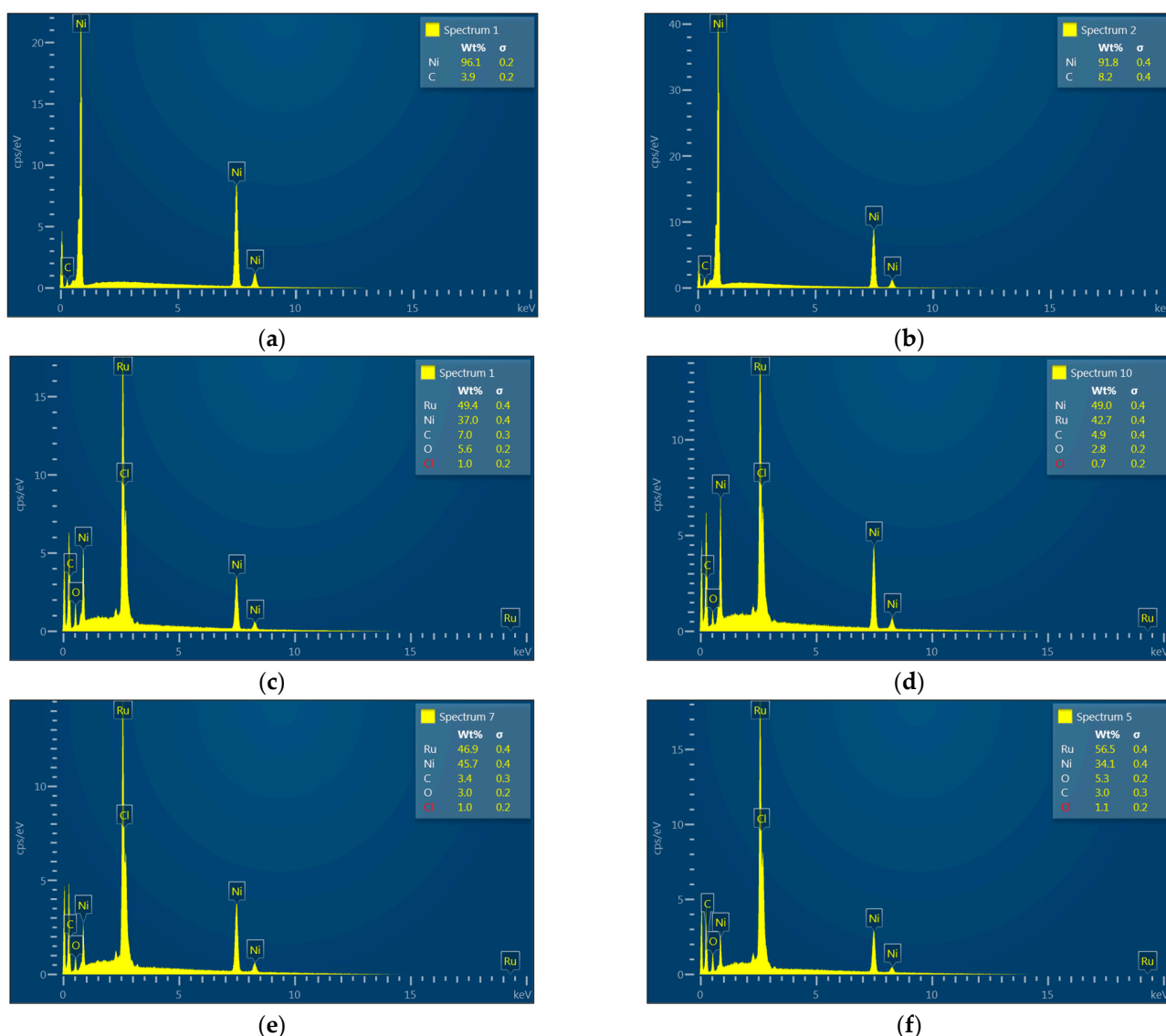
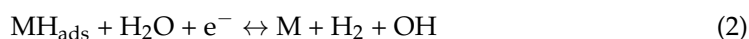


Figure 4. EDS spectra of (a) pristine NF, (b) NF*, (c) Ru/NF*, (d) Ru/NF*-A, (e) Ru/NF*-AH, and (f) Ru/NF*-AO.

3.5. Evaluation of Electrocatalytic Activity

3.5.1. KOH Electrolyte

Figure 5 and Table 2 show the results of the electrochemical HER activity evaluated in 1 M KOH aqueous solution. Principally, the HER mechanism in a highly alkaline medium is described by the following three equations:



where M indicates metal and H_{ads} indicates adsorbed hydrogen. Reaction (1) (Volmer step) represents the electroreduction of water molecules by hydrogen adsorption onto the electrode; reaction (2) (Heyrovsky step) represents the electrochemical hydrogen desorption process, and reaction (3) (Tafel step) represents the production of H₂ by chemical desorption of absorbed hydrogen atoms [35–37].

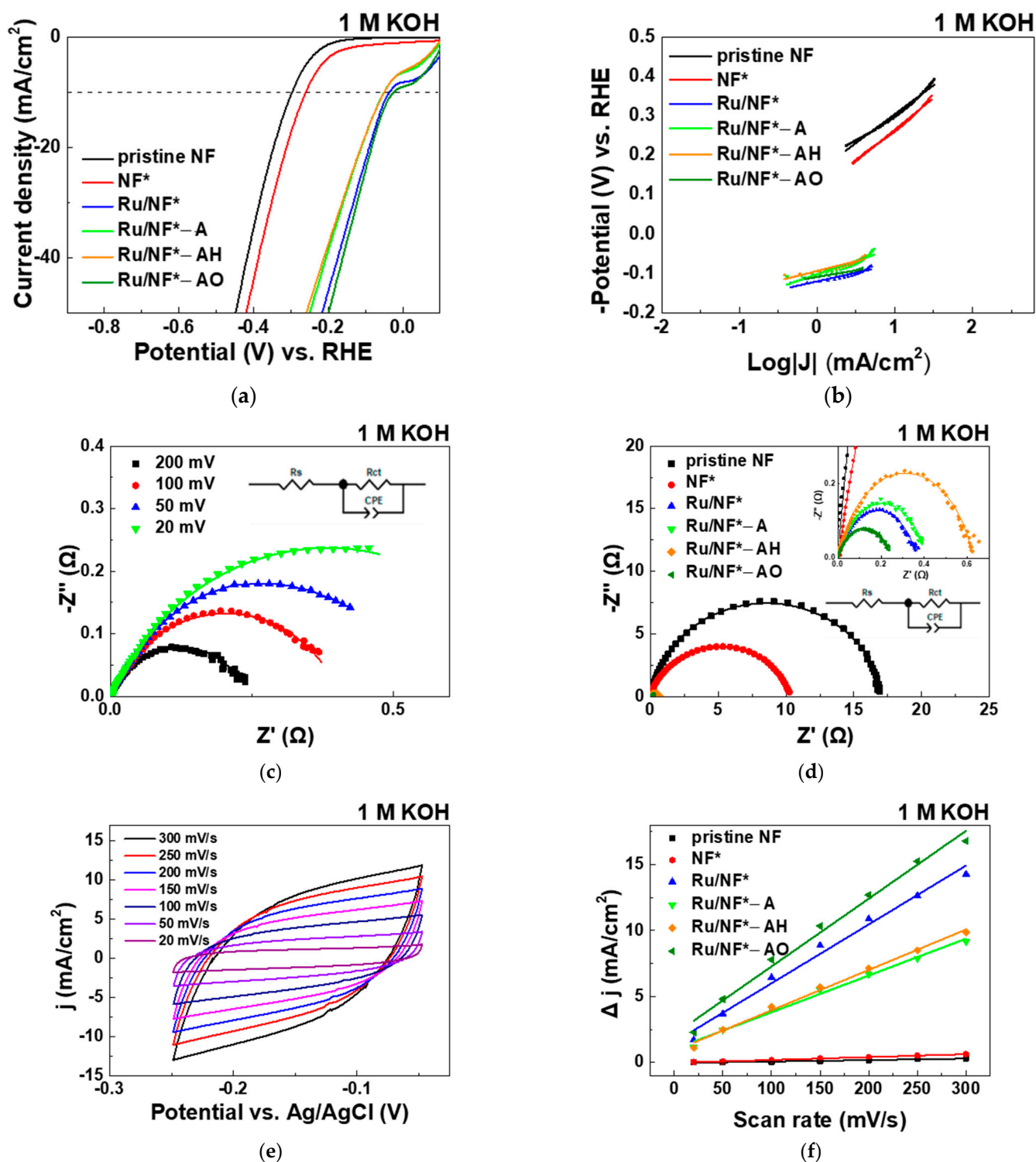


Figure 5. In 1 M KOH aqueous solution: (a) LSV polarization curves of pristine NF, NF*, Ru/NF*, Ru/NF*-A, Ru/NF*-AH, and Ru/NF*-AO catalysts toward HER. (b) Corresponding Tafel plots of HER. (c) Nyquist plots of Ru/NF*-AO catalyst at four different applied overpotentials versus RHE. (d) Nyquist plots of pristine NF, NF*, Ru/NF*, Ru/NF*-A, Ru/NF*-AH, and Ru/NF*-AO catalysts at an overpotential of 200 mV versus RHE. (e) CV potential curves of Ru/NF*-AO at different scan rates. (f) Current density of various electrocatalysts as a function of scan rate.

Table 2. Corresponding parameters of electrocatalyst in 1M KOH as calculated from Figure 5.

| Electrocatalyst | Overpotential (mV) @Current Density 10 mA/cm ² | Tafel Slope (mV/dec) | R _{ct} (Ω) | 2C _{dl} (mF/cm ²) |
|-----------------|---|-------------------------|------------------------|---|
| Pristine NF | 299 | 147 | 17.1 | 1.12 |
| NF* | 260 | 161 | 10.3 | 2.19 |
| Ru/NF* | 36 | 44 | 0.4 | 44.60 |
| Ru/NF*-A | 50 | 68 | 0.4 | 27.85 |
| Ru/NF*-AH | 50 | 49 | 0.6 | 30.61 |
| Ru/NF*-AO | 25 | 33 | 0.2 | 51.41 |

After cleaning procedure with 0.1 M H₂SO₄, DI water, alcohol, and ACE. A: Plasma treatment with 100% Ar. AH: Plasma treatment with 95% Ar–5% H₂. AO: Plasma treatment with 95% Ar–5% O₂.

The LSV polarization curves of the pristine NF and NF* indicate overpotentials of 299 and 260 mV at 10 mA/cm², respectively (Figure 5a and Table 2). The corresponding Tafel slopes are 147 and 161 mV/dec, as shown in Figure 5b. After depositing Ru, the overpotentials significantly decreased. The overpotential at 10 mA/cm² further decreased from 36 to 25 mV with 95% Ar–5% O₂ plasma treatment (sample Ru/NF*-AO). The Tafel slope of Ru/NF*-AO is 33 mV/dec. The HER kinetics follow the Volmer–Tafel mechanism [38,39].

To characterize the electrode/electrolyte interface and the corresponding processes, EIS measurements were performed at different selected overpotentials: 20, 50, 100, and 200 mV. At a cathodic overpotential of 20 mV, hydrogen evolution does not begin; at those of 50 mV and 100 mV, hydrogen production occurs at a very low rate; and at that of 200 mV, hydrogen is energetically generated [40]. Figure 5c presents the Nyquist plots of the Ru/NF*-AO catalyst at overpotentials of 200, 100, 50, and 20 mV versus RHE; the equivalent electrical circuit is shown in the inset. In the model circuit, R_s is the series resistance, R_{ct} is the charge-transfer resistance and CPE is the constant-phase element. The impedance properties are similar at different HER overpotentials, as shown in Figure 5c, suggesting the occurrence of similar electrochemical processes at all these overpotentials [41]. The results show that the electron transfer kinetics of the HER is faster with increasing overpotential, which is in accordance with the obtained polarization curves.

Figure 5d shows the Nyquist plots of pristine NF, NF*, Ru/NF*, Ru/NF*-A, Ru/NF*-AH, and Ru/NF*-AO catalysts in 1 M KOH at an overpotential of 200 mV vs. RHE; the inset shows magnified views of these plots. The R_{ct} values for Ru/NF*, Ru/NF*-A, Ru/NF*-AH, and Ru/NF*-AO are 0.4, 0.4, 0.6, and 0.2 Ω, respectively; these are much lower than those of pristine NF (17.1 Ω at an overpotential of 200 mV) and NF* (10.3 Ω at an overpotential of 200 mV). This implies a low charge-transfer resistance and highly efficient electron transport in all Ru-coated NF samples. Furthermore, the Ru/NF*-AO catalyst shows the lowest R_{ct} value, suggesting that the oxygen-containing plasma most significantly reduces the interfacial impedance.

Figure 5e shows the cyclic voltammetry (CV) potential curves of Ru/NF*-AO at scan rates of 20–300 mV/s. Figure 5f and Table 2 show the corresponding parameters for two times the double-layer capacitance (C_{dl}) of the catalyst. The fitting linear slope is equivalent to that of two times the C_{dl} value [42,43]; it is frequently used to express the electrochemical surface area (ECSA) [44–46]. The C_{dl} value of NF* is increased nearly twofold compared to that of pristine NF. In addition, the C_{dl} of the catalyst was significantly improved after Ru deposition. A value of 95% Ar–5% O₂ plasma treatment further increased the C_{dl} value and ECSA.

Previous studies have demonstrated that oxygen-containing plasma treatment could incorporate oxygen species into the surface with increased polarity [10,47]. This might explain why the electrocatalyst treated with oxygen-containing plasma has better performance in 1 M KOH aqueous solution. Furthermore, Ru catalysts with a small amount of lattice oxygen offer more suitable binding energies of oxygen intermediates for optimal activity [48]. These results reflect those of Yuanli et al. (2021) [49] who also found enriched defects in the surface-introduced lattice oxygen in the subsurface of Ru, leading to the

overall optimization of the electronic structure and coordination environment of the active sites. The Ru surface model not only weakens the bonding strength of the catalyst and H but also accelerates water molecule dissociation. This can greatly contribute toward obtaining excellent HER activity. In accordance with the above results, the oxygen plasma treatment causing surface defects or a slight oxidation reaction is suggested to enhance the HER activity.

3.5.2. PBS and H₂SO₄ Electrolyte

Figure 6 and Table 3 show the electrochemical HER activity evaluated in 0.1 M PBS aqueous solution. Figure 7 and Table 4 shows the electrochemical HER activity in evaluated in 0.5 M H₂SO₄ aqueous solution. In 0.1 M PBS aqueous solution, the pristine NF, NF*, Ru/NF*, Ru/NF*-A, Ru/NF*-AH, and Ru/NF*-AO showed overpotentials (at 10 mA/cm²) of 617, 544, 300, 320, 300, and 281 mV, respectively (Figure 6a). In 0.5 M H₂SO₄ aqueous solution (Figure 7a), the pristine NF, NF*, Ru/NF*, Ru/NF*-A, Ru/NF*-AH, and Ru/NF*-AO show overpotentials (at 10 mA/cm²) of 291, 243, 94, 89, 87, and 86 mV, respectively. The overpotential decreased after H₂SO₄ cleaning. Similar to the case of 1 M KOH solution, Ru deposition also reduced the overpotential significantly in 0.1 M PBS and 0.5 M H₂SO₄ solutions. Oxygen-containing (95% Ar–5% O₂) plasma treatment also produced electrodes with the smallest overpotential in these two cases.

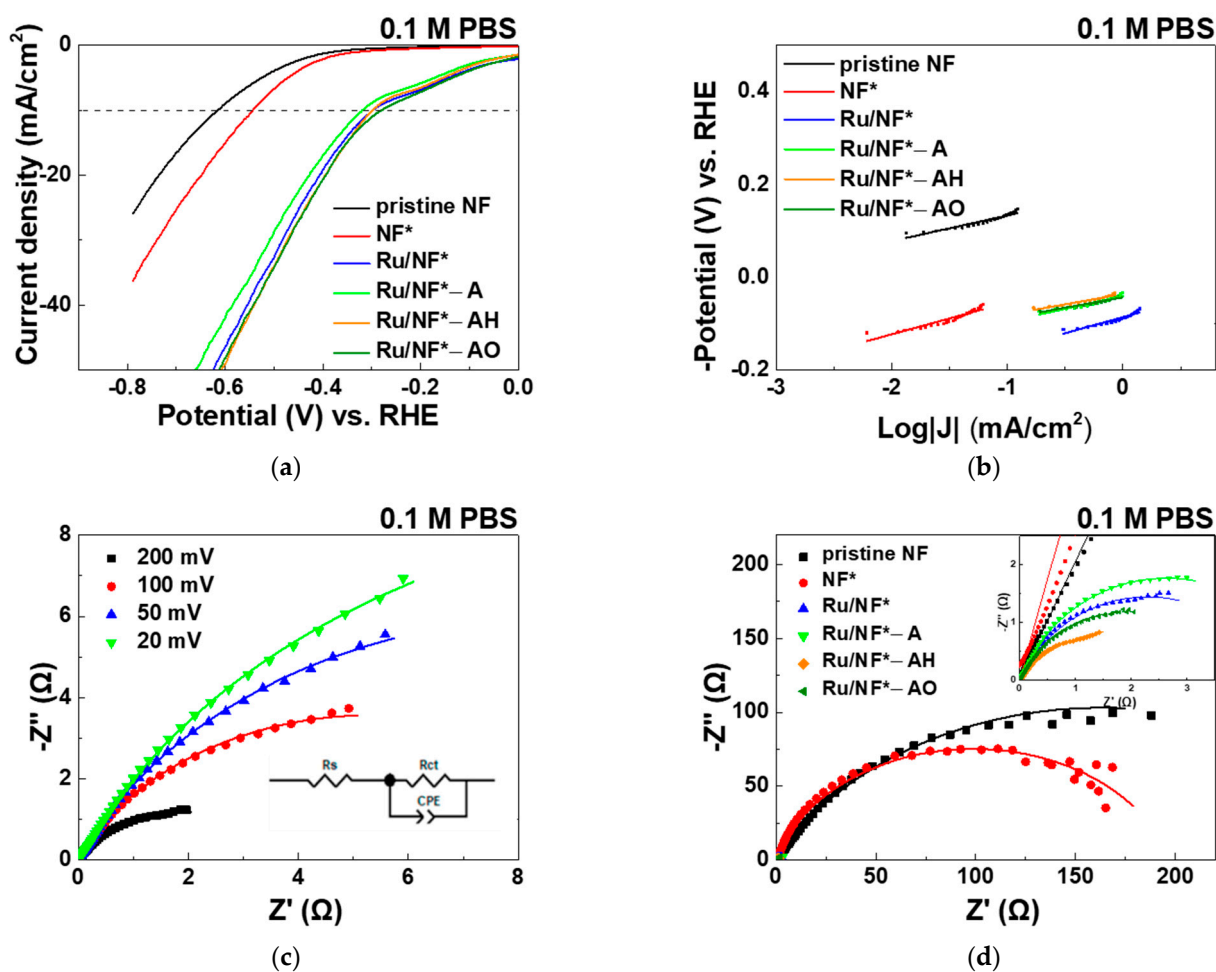


Figure 6. In 0.1 M PBS aqueous solution: (a) LSV polarization curves of pristine NF, NF*, Ru/NF*, Ru/NF*-A, Ru/NF*-AH, and Ru/NF*-AO toward HER. (b) Corresponding Tafel plots of HER. (c) Nyquist plots of the Ru/NF*-AO catalyst at four different applied overpotentials versus RHE. (d) Nyquist plots of pristine NF, NF*, Ru/NF*, Ru/NF*-A, Ru/NF*-AH, and Ru/NF*-AO catalysts at an overpotential of 200 mV versus RHE.

Table 3. Corresponding parameters of electrocatalysts in 0.1 M PBS as calculated from Figure 6.

| Electrocatalyst | Overpotential (mV) @ Current Density 10 mA/cm ² | Tafel Slope (mV/dec) | R _{ct} (Ω) |
|-----------------|--|-------------------------|------------------------|
| pristine NF | 617 | 56 | 327.2 |
| NF* | 544 | 68 | 197.2 |
| Ru/NF* | 300 | 69 | 4.6 |
| Ru/NF*-A | 320 | 55 | 5.3 |
| Ru/NF*-AH | 300 | 45 | 3.5 |
| Ru/NF*-AO | 281 | 45 | 3.9 |

After cleaning procedure with 0.1 M H₂SO₄, DI water, alcohol, and ACE. A: Plasma treatment with 100% Ar. AH: Plasma treatment with 95% Ar-5% H₂. AO: Plasma treatment with 95% Ar-5% O₂.

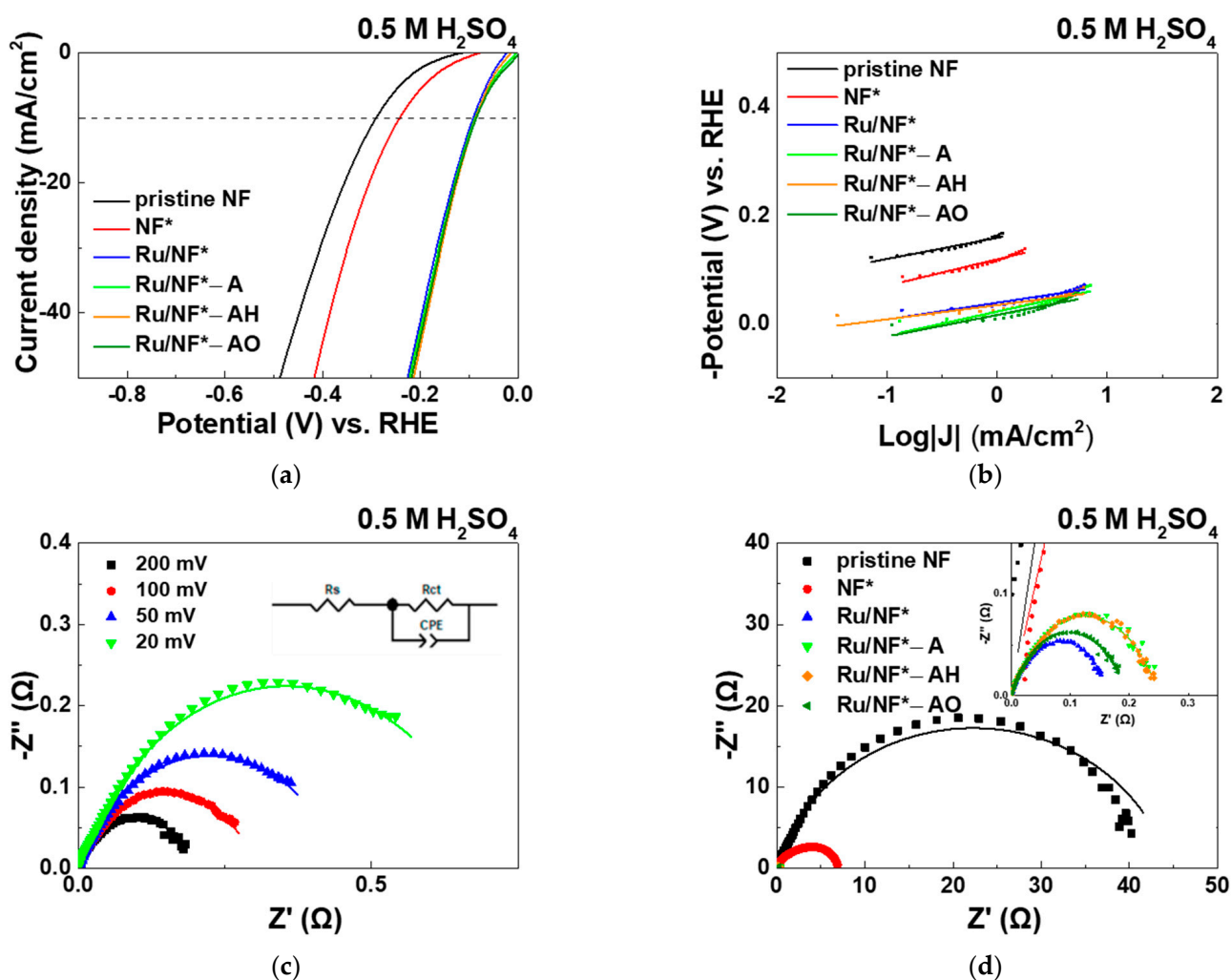


Figure 7. In 0.5 M H₂SO₄ aqueous solution: (a) LSV polarization curves of pristine NF, NF*, Ru/NF*, Ru/NF*-A, Ru/NF*-AH, and Ru/NF*-AO catalysts toward HER. (b) Corresponding Tafel plots of HER. (c) Nyquist plots of the Ru/NF*-AO catalyst at four different applied overpotentials versus RHE. (d) Nyquist plots of pristine NF, NF*, Ru/NF*, Ru/NF*-A, Ru/NF*-AH, and Ru/NF*-AO catalysts at an overpotential of 200 mV versus RHE.

Table 4. The corresponding parameters of the electrocatalyst in 0.5 M H₂SO₄ aqueous solution calculated from Figure 7.

| Electrocatalyst | Overpotential (mV) @ Current Density 10 mA/cm ² | Tafel Slope (mV/dec) | R _{ct} (Ω) |
|-----------------|--|-------------------------|------------------------|
| pristine NF | 291 | 39 | 44.6 |
| NF* | 243 | 49 | 7.3 |
| Ru/NF* | 94 | 31 | 0.2 |
| Ru/NF*-A | 89 | 23 | 0.3 |
| Ru/NF*-AH | 87 | 35 | 0.3 |
| Ru/NF*-AO | 86 | 26 | 0.2 |

After cleaning procedure with 0.1 M H₂SO₄, DI water, alcohol, and ACE. A: Plasma treatment with 100% Ar. AH: Plasma treatment with 95% Ar–5% H₂. AO: Plasma treatment with 95% Ar–5% O₂.

In neutral aqueous solution, the water molecules are first dissociated to generate hydrogen atoms adsorbed onto the surface of the electrode, and then, the hydrogen atoms evolve to form H₂ molecules [5,50]. Unlike in alkaline media, protons play an important role as a source for generating hydrogen molecules in acidic media, as indicated by the following three equations: Volmer: H⁺ + M + e[−] → MH_{ads}; Heyrovsky: MH_{ads} + H⁺ + e[−] → M + H₂ and Tafel: 2MH_{ads} → 2M + H₂ [5,51]. The Tafel slope of pristine NF, NF*, Ru/NF*, Ru/NF*-A, Ru/NF*-AH and Ru/NF*-AO for neutral HER was in the interval of 45–69 mV/dec (Figure 6b), corresponding to a typical Volmer–Heyrovsky HER mechanism in which the electrochemical recombination represents the rate-determining step [5]. Moreover, the Tafel slope of the pristine Ru/NF*, Ru/NF*-A, Ru/NF*-AH, and Ru/NF*-AO in acidic media was approximately 30 mV/dec (Figure 7b), corresponding to a typical Volmer–Tafel HER mechanism.

To provide further insight into the relative enhancement of the HER catalytic activity for the Ru/NF*-AO catalyst, EIS analysis was performed at various HER overpotentials (20–200 mV) in 0.1 M PBS and 0.5 M H₂SO₄ aqueous solutions, and the Nyquist plots of the EIS responses are shown in Figures 6c and 7c. As the overpotential increases, the R_{ct} decreases. The Nyquist plots of pristine NF, NF*, Ru/NF*, Ru/NF*-A, Ru/NF*-AH, and Ru/NF*-AO catalysts at an overpotential of 200 mV are shown in Figures 6d and 7d. R_{ct} value was significantly decreased after cleaning with H₂SO₄ and depositing a Ru layer, in good agreement with the overpotential results. A lower R_{ct} value usually indicates faster electron transfer between electrocatalyst–electrolyte interface [41]. In 0.1 M PBS and 0.5 M H₂SO₄ aqueous solutions, Ru/NF* electrocatalysis changes slightly after three types of plasma treatments, as indicated by the R_{ct} values and overpotentials.

The long-term durability of Ru/NF*-AO in alkaline, neutral, and acidic solution was tested through LSV measurement, as shown in Figure S5. The overpotential at 10 mA/cm² was stable during the measurement in alkaline and neutral solutions. The Ru/NF*-AO catalyst showed excellent durability and overpotential decay of approximately 29 and 22 mV after 12 h in 1 M KOH and 0.1 M PBS, respectively. Compared with the decay in 1 M KOH and 0.1 M PBS aqueous solutions, that in the 0.5 M H₂SO₄ aqueous solution was slightly higher, probably because of the corrosion of the electrode in acid.

4. Conclusions

Low-pressure 95% Ar–5% H₂, pure Ar, and 95% Ar–5% O₂ plasmas are used for post-treating Ru/NF. Ru/NF is then tested as a catalyst for HER. The overpotential at 10 mA/cm² decreased from 36 to 25 mV with 95% Ar–5% O₂ plasma treatment in alkaline solution. A low Tafel slope of 33 mV/dec was achieved under the Heyrovsky–Tafel mechanism of HER kinetics after oxygen-containing plasma treatment. The EIS results also indicate that 95% Ar–5% O₂ plasma treatment significantly decreases the charge-transfer resistance, in agreement with the overpotential result. The Ru/NF*-AO catalyst showed excellent durability and overpotential decay of ~29 mV after 12 h in 1 M KOH.

Supplementary Materials: The following supporting information can be downloaded at: <https://www.mdpi.com/article/10.3390/ma15072603/s1>, Figure S1: XPS spectra of C1s for the catalytic activity of (a) pristine NF, (b) NF*, (c) Ru/NF*, (d) Ru/NF*-A, (e) Ru/NF*-AH, (f) Ru/NF*-AO.; Figure S2: XPS spectra of Ru3d for the catalytic activity of (a) pristine NF, (b) NF*, (c) Ru/NF*, (d) Ru/NF*-A, (e) Ru/NF*-AH, (f) Ru/NF*-AO.; Figure S3: XPS spectra of O1s for the catalytic activity of (a) pristine NF, (b) NF*, (c) Ru/NF*, (d) Ru/NF*-A, (e) Ru/NF*-AH, (f) Ru/NF*-AO.; Figure S4: XPS spectra of Ni2p for the catalytic activity of (a) pristine NF, (b) NF*, (c) Ru/NF*, (d) Ru/NF*-A, (e) Ru/NF*-AH, (f) Ru/NF*-AO.; Figure S5: LSV polarization curves for HER catalyzed by Ru/NF*-AO before and after a durability test in (a) 1 M KOH, (a) 0.1 M PBS, and (c) 0.5 M H2SO4 aqueous solution.

Author Contributions: Conceptualization, J.-Z.C. and I.-C.C.; methodology, J.-Z.C. and I.-C.C.; software, C.L.; validation, C.L., C.-Y.T. and Y.-C.W.; formal analysis, C.L.; validation, C.L., C.-Y.T. and Y.-C.W.; investigation, C.L. and C.-Y.T.; resources, J.-Z.C. and I.-C.C.; data curation, C.L. and C.-Y.T.; writing—original draft preparation, C.L.; writing—review and editing, J.-Z.C.; visualization, J.-Z.C.; supervision, J.-Z.C. and I.-C.C.; project administration, J.-Z.C. and I.-C.C.; funding acquisition, J.-Z.C. and I.-C.C. All authors have read and agreed to the published version of the manuscript.

Funding: This work is supported by the Ministry of Science and Technology in Taiwan under grant no. MOST 110-3116-F-002-002. J.-Z.C. gratefully acknowledges funding supports by the ‘Advanced Research Center for Green Materials Science and Technology’ from the Featured Area Research Center Program of the Higher Education Sprout Project by the Ministry of Education (110L9006) and the Ministry of Science and Technology in Taiwan (MOST 110-2634-F-002-043 and MOST 108-2221-E-002-088-MY3).

Institutional Review Board Statement: Not applicable.

Informed Consent Statement: Not applicable.

Data Availability Statement: Not applicable.

Conflicts of Interest: The authors declare no conflict of interest.

References

1. Van der Hoeven, M. *World Energy Outlook 2012*; International Energy Agency: Tokyo, Japan, 2013.
2. OECD; IEA. *Energy and Air Pollution: World Energy Outlook Special Report 2016*; International Energy Agency: Paris, France, 2016.
3. Shi, Y.; Zhang, B. Correction: Recent advances in transition metal phosphide nanomaterials: Synthesis and applications in hydrogen evolution reaction. *Chem. Soc. Rev.* **2016**, *45*, 1781. [[CrossRef](#)] [[PubMed](#)]
4. Jiang, P.; Yang, Y.; Shi, R.; Xia, G.; Chen, J.; Su, J.; Chen, Q. Pt-like electrocatalytic behavior of Ru–MoO₂ nanocomposites for the hydrogen evolution reaction. *J. Mater. Chem. A* **2017**, *5*, 5475–5485. [[CrossRef](#)]
5. Xia, J.; Volokh, M.; Peng, G.; Fu, Y.; Wang, X.; Shalom, M. Low-cost porous ruthenium layer deposited on nickel foam as a highly active universal-pH electrocatalyst for the hydrogen evolution reaction. *ChemSusChem* **2019**, *12*, 2780–2787. [[CrossRef](#)] [[PubMed](#)]
6. Wang, J.; Wei, Z.; Mao, S.; Li, H.; Wang, Y. Highly uniform Ru nanoparticles over N-doped carbon: pH and temperature-universal hydrogen release from water reduction. *Energy Environ. Sci.* **2018**, *11*, 800–806. [[CrossRef](#)]
7. Li, Y.; Zhang, L.; Qin, Y.; Chu, F.; Kong, Y.; Tao, Y.; Li, Y.; Bu, Y.; Ding, D.; Liu, M. Crystallinity dependence of ruthenium nanocatalyst toward hydrogen evolution reaction. *ACS Catal.* **2018**, *8*, 5714–5720. [[CrossRef](#)]
8. Zhang, C.; Jiang, L.; Zhang, Y.; Hu, J.; Leung, M.K. Janus effect of O₂ plasma modification on the electrocatalytic hydrogen evolution reaction of MoS₂. *J. Catal.* **2018**, *361*, 384–392. [[CrossRef](#)]
9. Li, S.; Zhou, S.; Wang, X.; Tang, P.; Pasta, M.; Warner, J.H. Increasing the electrochemical activity of basal plane sites in porous 3D edge rich MoS₂ thin films for the hydrogen evolution reaction. *Mater. Today Energy* **2019**, *13*, 134–144. [[CrossRef](#)]
10. Tao, L.; Duan, X.; Wang, C.; Duan, X.; Wang, S. Plasma-engineered MoS₂ thin-film as an efficient electrocatalyst for hydrogen evolution reaction. *Chem. Commun.* **2015**, *51*, 7470–7473. [[CrossRef](#)]
11. Zhang, T.; Wu, J.; Chen, J.; Pan, Q.; Wang, X.; Zhong, H.; Tao, R.; Yan, J.; Hu, Y.; Ye, X.; et al. Activating titanium metal with H₂ plasma for the hydrogen evolution reaction. *ACS Appl. Mater. Interfaces* **2021**, *13*, 24682–24691. [[CrossRef](#)]
12. Wang, C.; Jiang, J.; Ding, T.; Chen, G.; Xu, W.; Yang, Q. Monodisperse ternary NiCoP nanostructures as a bifunctional electrocatalyst for both hydrogen and oxygen evolution reactions with excellent performance. *Adv. Mater. Interfaces* **2016**, *3*, 1500454. [[CrossRef](#)]
13. Jiang, N.; You, B.; Sheng, M.; Sun, Y. Electrodeposited cobalt-phosphorous-derived films as competent bifunctional catalysts for overall water splitting. *Angew. Chem.* **2015**, *127*, 6349–6352. [[CrossRef](#)]
14. Zhu, Y.-P.; Liu, Y.-P.; Ren, T.-Z.; Yuan, Z.-Y. Self-supported cobalt phosphide mesoporous nanorod arrays: A flexible and bifunctional electrode for highly active electrocatalytic water reduction and oxidation. *Adv. Funct. Mater.* **2015**, *25*, 7337–7347. [[CrossRef](#)]

15. Liu, B.; Zhang, L.; Xiong, W.; Ma, M. Cobalt-nanocrystal-assembled hollow nanoparticles for electrocatalytic hydrogen generation from neutral-pH water. *Angew. Chem.* **2016**, *128*, 6837–6841. [[CrossRef](#)]
16. Harnisch, F.; Sievers, G.; Schröder, U. Tungsten carbide as electrocatalyst for the hydrogen evolution reaction in pH neutral electrolyte solutions. *Appl. Catal. B Environ.* **2009**, *89*, 455–458. [[CrossRef](#)]
17. Popczun, E.J.; Read, C.G.; Roske, C.W.; Lewis, N.S.; Schaak, R.E. Highly active electrocatalysis of the hydrogen evolution reaction by cobalt phosphide nanoparticles. *Angew. Chem. Int. Ed.* **2014**, *53*, 5427–5430. [[CrossRef](#)] [[PubMed](#)]
18. Jiang, P.; Liu, Q.; Liang, Y.; Tian, J.; Asiri, A.M.; Sun, X. A cost-effective 3D hydrogen evolution cathode with high catalytic activity: FeP nanowire array as the active phase. *Angew. Chem.* **2014**, *126*, 13069–13073. [[CrossRef](#)]
19. Han, S.; Feng, Y.; Zhang, F.; Yang, C.; Yao, Z.; Zhao, W.; Qiu, F.; Yang, L.; Yao, Y.; Zhuang, X.; et al. Metal-phosphide-containing porous carbons derived from an ionic-polymer framework and applied as highly efficient electrochemical catalysts for water splitting. *Adv. Funct. Mater.* **2015**, *25*, 3899–3906. [[CrossRef](#)]
20. Vrubel, H.; Hu, X. Molybdenum boride and carbide catalyze hydrogen evolution in both acidic and basic solutions. *Angew. Chem. Int. Ed.* **2012**, *51*, 12703–12706.
21. Gao, M.-R.; Liang, J.-X.; Zheng, Y.-R.; Xu, Y.-F.; Jiang, J.; Gao, Q.; Li, J.; Yu, S.-H. An efficient molybdenum disulfide/cobalt diselenide hybrid catalyst for electrochemical hydrogen generation. *Nat. Commun.* **2015**, *6*, 5982. [[CrossRef](#)]
22. Zhang, B.; Lui, Y.H.; Gaur, A.P.S.; Chen, B.; Tang, X.; Qi, Z.; Hu, S. Hierarchical FeNiP@Ultrathin Carbon Nanoflakes as Alkaline Oxygen Evolution and Acidic Hydrogen Evolution Catalyst for Efficient Water Electrolysis and Organic Decomposition. *ACS Appl. Mater. Interfaces* **2018**, *10*, 8739–8748. [[CrossRef](#)]
23. Wang, D.-Y.; Gong, M.; Chou, H.-L.; Pan, C.-J.; Chen, H.-A.; Wu, Y.; Lin, M.-C.; Guan, M.; Yang, J.; Chen, C.-W.; et al. Highly active and stable hybrid catalyst of cobalt-doped Fe₂S nanosheets–carbon nanotubes for hydrogen evolution reaction. *J. Am. Chem. Soc.* **2015**, *137*, 1587–1592. [[CrossRef](#)] [[PubMed](#)]
24. Chen, W.-F.; Sasaki, K.; Ma, C.; Frenkel, A.I.; Marinkovic, N.; Muckerman, J.T.; Zhu, Y.; Adzic, R.R. Hydrogen-evolution catalysts based on non-noble metal nickel–molybdenum nitride nanosheets. *Angew. Chem. Int. Ed.* **2012**, *51*, 6131–6135. [[CrossRef](#)] [[PubMed](#)]
25. Mahmood, N.; Yao, Y.; Zhang, J.-W.; Pan, L.; Zhang, X.; Zou, J.-J. Electrocatalysts for Hydrogen evolution in alkaline electrolytes: Mechanisms, challenges, and prospective solutions. *Adv. Sci.* **2018**, *5*, 1700464. [[CrossRef](#)] [[PubMed](#)]
26. Tian, J.; Liu, Q.; Asiri, A.M.; Sun, X. Self-supported nanoporous cobalt phosphide nanowire arrays: An efficient 3D hydrogen-evolving cathode over the wide range of pH 0–14. *J. Am. Chem. Soc.* **2014**, *136*, 7587–7590. [[CrossRef](#)]
27. Ye, R.; Liu, Y.; Peng, Z.; Wang, T.; Jalilov, A.S.; Jakobson, B.I.; Wei, S.-H.; Tour, J.M. High performance electrocatalytic reaction of hydrogen and oxygen on ruthenium nanoclusters. *ACS Appl. Mater. Interfaces* **2017**, *9*, 3785–3791. [[CrossRef](#)]
28. Ledezma-Yanez, I.; Wallace, W.D.Z.; Sebastián-Pascual, P.; Climent, V.; Feliu, J.M.; Koper, M.T.M. Interfacial water reorganization as a pH-dependent descriptor of the hydrogen evolution rate on platinum electrodes. *Nat. Energy* **2017**, *2*, 17031. [[CrossRef](#)]
29. Huang, L.; Hou, Y.; Yu, Z.; Peng, Z.; Wang, L.; Huang, J.; Zhang, B.; Qian, L.; Wu, L.; Li, Z. Pt/Fe-NF electrode with high double-layer capacitance for efficient hydrogen evolution reaction in alkaline media. *Int. J. Hydrogen Energy* **2017**, *42*, 9458–9466. [[CrossRef](#)]
30. Lotfi, N.; Shahrabi, T.; Darband, G.B. Electrodeposition of cedar leaf-like graphene Oxide@Ni–Cu@Ni foam electrode as a highly efficient and ultra-stable catalyst for hydrogen evolution reaction. *Electrochim. Acta* **2019**, *326*, 134949. [[CrossRef](#)]
31. Chen, D.; Liu, Z. Dual-axial gradient doping (Zr and Sn) on hematite for promoting charge separation in photoelectrochemical water splitting. *ChemSusChem* **2018**, *11*, 3438–3448. [[CrossRef](#)]
32. Tseng, C.-H.; Hsin, J.-C.; Tsai, J.-H.; Chen, J.-Z. Dielectric-barrier-discharge jet treated flexible supercapacitors with carbon cloth current collectors of long-lasting hydrophilicity. *J. Electrochem. Soc.* **2020**, *167*, 116511. [[CrossRef](#)]
33. Xia, J.; He, G.; Zhang, L.; Sun, X.; Wang, X. Hydrogenation of nitrophenols catalyzed by carbon black-supported nickel nanoparticles under mild conditions. *Appl. Catal. B Environ.* **2016**, *180*, 408–415. [[CrossRef](#)]
34. Demir, E.; Akbayrak, S.; Önal, A.M.; Özkar, S. Nanoceria-supported ruthenium(0) nanoparticles: Highly active and stable catalysts for hydrogen evolution from water. *ACS Appl. Mater. Interfaces* **2018**, *10*, 6299–6308. [[CrossRef](#)] [[PubMed](#)]
35. Safizadeh, F.; Ghali, E.; Houlachi, G. Electrocatalysis developments for hydrogen evolution reaction in alkaline solutions—A review. *Int. J. Hydrogen Energy* **2015**, *40*, 256–274. [[CrossRef](#)]
36. Choquette, Y.; Brossard, L.; Lasia, A.; Menard, H. Study of the kinetics of hydrogen evolution reaction on Raney Nickel composite-coated electrode by AC impedance technique. *J. Electrochem. Soc.* **1990**, *137*, 1723–1730. [[CrossRef](#)]
37. Lasia, A.; Rami, A. Kinetics of hydrogen evolution on nickel electrodes. *J. Electroanal. Chem. Interfacial Electrochem.* **1990**, *294*, 123–141. [[CrossRef](#)]
38. Zhang, R.; Wang, X.; Yu, S.; Wen, T.; Zhu, X.; Yang, F.; Sun, X.; Wang, X.; Hu, W. Ternary NiCo₂P_x nanowires as pH-universal electrocatalysts for highly efficient hydrogen evolution reaction. *Adv. Mater.* **2017**, *29*, 1605502. [[CrossRef](#)]
39. Gao, K.; Wang, Y.; Wang, Z.; Zhu, Z.; Wang, J.; Luo, Z.; Zhang, C.; Huang, X.; Zhang, H.; Huang, W. Ru nanodendrites composed of ultrathin fcc/hcp nanoblades for the hydrogen evolution reaction in alkaline solutions. *Chem. Commun.* **2018**, *54*, 4613–4616. [[CrossRef](#)]
40. Herraiz-Cardona, I.; Ortega, E.; Antón, J.G.; Pérez-Herranz, V. Assessment of the roughness factor effect and the intrinsic catalytic activity for hydrogen evolution reaction on Ni-based electrodeposits. *Int. J. Hydrogen Energy* **2011**, *36*, 9428–9438. [[CrossRef](#)]

41. Huang, Y.; Ge, J.; Hu, J.; Zhang, J.; Hao, J.; Wei, Y. Nitrogen-doped porous molybdenum carbide and phosphide hybrids on a carbon matrix as highly effective electrocatalysts for the hydrogen evolution reaction. *Adv. Energy Mater.* **2018**, *8*, 1701601. [[CrossRef](#)]
42. Sun, F.; Wang, G.; Ding, Y.; Wang, C.; Yuan, B.; Lin, Y. NiFe-based metal–Organic framework nanosheets directly supported on nickel foam acting as robust electrodes for electrochemical oxygen evolution reaction. *Adv. Energy Mater.* **2018**, *8*, 1800584. [[CrossRef](#)]
43. Raja, S.D.; Lin, H.-W.; Lu, S.-Y. Synergistically well-mixed MOFs grown on nickel foam as highly efficient durable bifunctional electrocatalysts for overall water splitting at high current densities. *Nano Energy* **2019**, *57*, 1800584.
44. Cai, W.; Chen, R.; Yang, H.; Tao, H.B.; Wang, H.-Y.; Gao, J.; Liu, W.; Liu, S.; Hung, S.-F.; Liu, B. Amorphous versus crystalline in water oxidation catalysis: A case study of NiFe alloy. *Nano Lett.* **2020**, *20*, 4278–4285. [[CrossRef](#)] [[PubMed](#)]
45. Zhang, Y.; Ouyang, B.; Xu, J.; Chen, S.; Rawat, R.S.; Fan, H.J. 3D porous hierarchical nickel–Molybdenum nitrides synthesized by RF plasma as highly active and stable hydrogen-evolution-reaction electrocatalysts. *Adv. Energy Mater.* **2016**, *6*, 1600221. [[CrossRef](#)]
46. Wu, H.B.; Xia, B.Y.; Yu, L.; Yu, X.-Y.; Lou, X.W. Porous molybdenum carbide nano-octahedrons synthesized via confined carburization in metal-organic frameworks for efficient hydrogen production. *Nat. Commun.* **2015**, *6*, 6512. [[CrossRef](#)] [[PubMed](#)]
47. Lu, Z.; Zhu, W.; Yu, X.; Zhang, H.; Li, Y.; Sun, X.; Wang, X.; Wang, H.; Wang, J.; Luo, J.; et al. Ultrahigh hydrogen evolution performance of under-water “superaerophobic” MoS₂ nanostructured electrodes. *Adv. Mater.* **2014**, *26*, 2683–2687. [[CrossRef](#)]
48. Li, Y.; Zhou, W.; Zhao, X.; Cheng, W.; Su, H.; Zhang, H.; Liu, M.; Liu, Q. Donutlike RuCu nanoalloy with ultrahigh mass activity for efficient and robust oxygen evolution in acid solution. *ACS Appl. Energy Mater.* **2019**, *2*, 7483–7489. [[CrossRef](#)]
49. Li, Y.; He, J.; Cheng, W.; Su, H.; Li, C.; Zhang, H.; Liu, M.; Zhou, W.; Chen, X.; Liu, Q. High mass-specific reactivity of a defect-enriched Ru electrocatalyst for hydrogen evolution in harsh alkaline and acidic media. *Sci. China Mater.* **2021**, *64*, 2467–2476. [[CrossRef](#)]
50. Zhang, Y.; Lei, H.; Duan, D.; Villota, E.; Liu, C.; Ruan, R. New insight into the mechanism of the hydrogen evolution reaction on MoP(001) from first principles. *ACS Appl. Mater. Interfaces* **2018**, *10*, 20429–20439. [[CrossRef](#)]
51. Yan, Y.; Xia, B.Y.; Zhao, B.; Wang, X. A review on noble-metal-free bifunctional heterogeneous catalysts for overall electrochemical water splitting. *J. Mater. Chem. A* **2016**, *4*, 17587–17603. [[CrossRef](#)]